

Electronic structure engineering of transition metal dichalcogenides for boosting hydrogen energy conversion electrocatalysts

Bing Hao(郝兵), Jingjing Guo(郭晶晶), Peizhi Liu(刘培植), and Junjie Guo(郭俊杰)

Citation: Chin. Phys. B, 2024, 33 (**9**): 096802. DOI: 10.1088/1674-1056/ad625b
Journal homepage: http://cpb.iphy.ac.cn; http://iopscience.iop.org/cpb

What follows is a list of articles you may be interested in

Symmetry quantification and segmentation in STEM imaging through Zernike moments

Jiadong Dan, Cheng Zhang, Xiaoxu Zhao(赵晓续), and N. Duane Loh
Chin. Phys. B, 2024, 33 (**8**): 086803. DOI: 10.1088/1674-1056/ad51f4

Anomalous strain effect in heteroepitaxial $SrRuO_3$ films on (111) $SrTiO_3$ substrates

Zhenzhen Wang(王珍珍), Weiheng Qi(戚炜恒), Jiachang Bi(毕佳畅), Xinyan Li(李欣岩), Yu Chen(陈雨), Fang Yang(杨芳), Yanwei Cao(曹彦伟), Lin Gu(谷林), Qinghua Zhang(张庆华), Huanhua Wang(王焕华), Jiandi Zhang(张坚地), Jiandong Guo(郭建东), and Xiaoran Liu(刘笑然)
Chin. Phys. B, 2022, 31 (**12**): 126801. DOI: 10.1088/1674-1056/ac8725

Fabrication of $GaAs/SiO_2/Si$ and GaAs/Si heterointerfaces by surface-activated chemical bonding at room temperature

Rui Huang(黄瑞), Tian Lan(兰天), Chong Li(李冲), Jing Li(李景), and Zhiyong Wang(王智勇)
Chin. Phys. B, 2021, 30 (**7**): 076802. DOI: 10.1088/1674-1056/abf917

High-resolution electron microscopy for heterogeneous catalysis research

Yong Zhu(朱勇), Mingquan Xu(许名权), Wu Zhou(周武)
Chin. Phys. B, 2018, 27 (**5**): 056804. DOI: 10.1088/1674-1056/27/5/056804

Aberration-corrected scanning transmission electron microscopy for complex transition metal oxides

Qing-Hua Zhang(张庆华), Dong-Dong Xiao(肖东东), Lin Gu(谷林)
Chin. Phys. B, 2016, 25 (**6**): 066803. DOI: 10.1088/1674-1056/25/6/066803

TOPICAL REVIEW — Stephen J. Pennycook: A research life in atomic-resolution STEM and EELS

Electronic structure engineering of transition metal dichalcogenides for boosting hydrogen energy conversion electrocatalysts

Bing Hao(郝兵), Jingjing Guo(郭晶晶), Peizhi Liu(刘培植)[†], and Junjie Guo(郭俊杰)[‡]

Key Laboratory of Interface Science and Engineering in Advanced Materials, Ministry of Education, Taiyuan University of Technology, Taiyuan 030024, *China*

(Received 29 April 2024; revised manuscript received 5 July 2024; accepted manuscript online 12 July 2024)

Electrocatalytic water splitting for hydrogen production is an appealing strategy to reduce carbon emissions and generate renewable fuels. This promising process, however, is limited by its sluggish reaction kinetics and high-cost catalysts. The two-dimensional (2D) transition metal dichalcogenides (TMDCs) have presented great potential as electrocatalytic materials due to their tunable bandgaps, abundant defective active sites, and good chemical stability. Consequently, phase engineering, defect engineering and interface engineering have been adopted to manipulate the electronic structure of TMDCs for boosting their exceptional catalytic performance. Particularly, it is essential to clarify the local structure of catalytically active sites of TMDCs and their structural evolution in catalytic reactions using atomic resolution electron microscopy and the booming *in situ* technologies, which is beneficial for exploring the underlying reaction mechanism. In this review, the growth regulation, characterization, particularly atomic configurations of active sites in TMDCs are summarized. The significant role of electron microscopy in the understanding of the growth mechanism, the controlled synthesis and functional optimization of 2D TMDCs are discussed. This review will shed light on the design and synthesis of novel electrocatalysts with high performance, as well as prompt the application of advanced electron microscopy in the research of materials science.

Keywords: TMDCs, STEM, hydrogen energy conversion, active site identification

PACS: 68.37.Ma, 88.30.–k, 71.23.–k, 73.22.–f **DOI:** 10.1088/1674-1056/ad625b

1. Introduction

Since the discovery of graphene in 2004,[1] various novel two-dimensional (2D) materials have been developed, like graphene derivatives,[2–4] hexagonal boron nitride,[5] metal oxides,[6–8] layered double hydroxides (LDHs)[9,10,12] and transition metal dichalcogenides (TMDCs).[13] TMDCs are a novel category of 2D materials with multiple phases ranging from insulators, semiconductors to conductors caused by the change of stacking configuration of their layered structure.[14] The structural diversity endows TMDCs novel physical properties such as excellent mechanical flexibility[15] and chemical stability, outstanding electronic and optical properties,[16] exceptional catalytic performance,[17] etc. Since several reviews covered the electronic properties and applications in various photonics and electronics,[13,18,19] it is therefore highly interesting to reveal the intrinsic correlation between the microstructure and the electrocatalytic performances of TMDC electrocatalysts in hydrogen energy conversion.

Hydrogen energy has been hailed as an ideal clean energy with the highest calorific value and the only by-production of water. Green hydrogen produced by water electrolysis using sustainable energy sources is currently an attractive alternative to overcome the energy and environmental crises of traditional fossil fuels.[20,21] However, hydrogen energy conversion processes, including hydrogen evolution reaction (HER), oxygen evolution reaction (OER), and oxidation reduction reaction (ORR), are limited by the sluggish reaction kinetics and call for highly efficient electrocatalysts.[4,22–24] The commercially used electrocatalysts are high-cost noble metal-based materials such as Pt/C, IrO_2, RuO_2, etc. In comparison with traditional precious metal materials, earth-abundant TMDC electrocatalysts exhibit comparable activities with much better economy based on their abundant catalytic active sites, tunable bandgaps and good chemical stability.[25] At present, phase engineering, defect engineering and interface engineering have been adopted to manipulate the electronic structure of TMDCs for boosting their exceptional catalytic performances.[26,27] Clarifying the atomic configurations of the active sites and catalytic mechanisms of TMDCs electrocatalyst, and thus achieving a controlled growth of TMDCs nanosheets with highly active phases and abundant active sites are the key issues to further improve the hydrogen energy conversion performances of TMDC catalysts.[28] The development of scanning transmission electron microscopy (STEM) has prompt it a compressive platform for the in-depth study of the crystal growth, phase identification, atomic configurations of nanostructures and interfaces. Along with the *in situ* techniques, structure evolutions of active sites during the reaction environment can be resolved in real time. Thus, the progress of advanced electron microscopy and the booming *in situ* technologies are of great significance for the design of high efficiency electrocatalysts, and thus facilitate the applica-

[†]Corresponding author. E-mail: liupeizhi@tyut.edu.cn
[‡]Corresponding author. E-mail: guojunjie@tyut.edu.cn

© 2024 Chinese Physical Society and IOP Publishing Ltd

tions of hydrogen energy.

Herein, the recent progresses in TMDCs for electrocatalysis, especially in HER, were summarized, along with the application of advanced STEM for the resolving of active site configurations. The highly efficient TMDC electrocatalysts with controllable manipulating strategies and the typical characteristic techniques were discussed first. Then we briefly introduced STEM and investigated its application in clarifying the catalytic active sites of TMDCs catalysts. In the end, perspectives on the current challenges and opportunities for TMDCs as novel electrocatalysts were provided. An outlook for the development and applications of STEM for future research in materials was presented. We hope the electronic structure tuning strategies and the corresponding clarification of active sites of TMDCs via advanced STEM will give some insights into designing novel materials for hydrogen energy conversion electrocatalysts and technologies.

2. Controllable synthesis of TMDCs

TMDCs can be expressed with a formula MX_2 (where $M =$ IVB–VIIB group metals, $X =$ chalcogen). A unit monolayer structure of MX_2 is constructed by a "sandwich" structure with X–MX bonding, in which the transition metal is sandwiched between two chalcogenide atoms and the bulk is bonded with van der Waals (vdW) force. Importantly, according to the arrangement of M and X atoms and the stacking order of the layers, various structural phases are formed, namely, 2H, 3R, 1T, 1T′ and $1T_d$ phases, and exhibit band structure variations from metal to insulator.[19] For example, the more electrocatalysis active 1T-MoS_2 occupying a tetragonal system with an octahedral coordination of metal atoms belongs to metallic phase, while the stable semiconductor 2H-MoS_2 is characterized as a hexagonal system with a trigonal prismatic coordination of metal atoms in each layer.[29] The high quality TMDCs are essential for novel 2D electronic devices, while specific defects such as vacancies and heteroatom doping introduced by the defect engineering are essential for the active sites as electrocatalysts, which calls for the controllable synthesis of TMDCs. The well-established preparation methods can be roughly divided into two categories of top-down and bottom-up strategies, including the mechanical exfoliation, chemical vapor deposition (CVD), and hydro/solvothermal method, which are introduced in this section.[30–32]

2.1. Exfoliation from the bulk materials

As a commonly used top-down preparation method, mechanical exfoliation technology has been widely used to prepare 2D materials, such as graphene,[33] black phosphorus,[34] and TMDCs.[35] With the advantages of simplicity and versatility, TMDCs nanosheets with large specific surface area and high crystalline quality can be obtained by exfoliating the bulk. Less than satisfactory, the exfoliated TMDCs with traditional mechanical stripping usually expose the basal crystal plane with limited active sites on the edge, which is not a highly active crystal plane for water electrolysis. In order to activate the basal plane, researchers have developed improved mechanical stripping technologies, such as oxygen plasma assisted stripping method, gold film assisted stripping method and electrochemical exfoliation, which are still vibrant in the basic research and application of 2D materials. Yang *et al.* obtained the $MoTe_2$ nanosheets by mechanical exfoliation following a laser irradiation, by which Te vacancies were introduced. Consequently, the electron delocalization around Mo atom and the upshift of the d-band center from -0.19 eV to -0.086 eV promoted the adsorption of hydrogen and activated the basal plane of the catalyst surface for HER catalysis.[36] Fu *et al.* (Figs. 1(a) and 1(b)) presented a one-step Ag-assisted method that can efficiently exfoliate many large-area 2D monolayers (e.g., MoS_2, WS_2, 1T-WTe_2, $MoSe_2$), with a comparable yield ratio and extended propagation of surface plasmonic polariton to those from Au-enhanced exfoliation method.[37] Hu *et al.* reported a facile and scalable solvent-free ball-milling approach to synthesis the nearly atom-layered MoS_2 nanosheets (ALMS), in which graphene quantum dots (GQDs) were employed as exfoliation agents (Figs. 1(c)–1(e)). The morphology and thickness of the nanosheets were measured with atomic force microscopy (AFM, Fig. 1(e)). The mechanochemical interaction promoted the combination of vertically aligned 2D MoS_2 and GQDs, which accelerated electron transfer in HER process, and thus resulted in an improved HER activity compared to the bulk MoS_2 catalyst.[38] As shown in Figs. 1(f)–1(h), the few-layer MoS_2 was obtained by a mild electrochemical exfoliation with a high anodic potential of 0.2 V–1.4 V applied to bulk MoS_2 in a 1 M zinc sulfate solution. The exfoliated few-layer MoS_2 was demonstrated to be more efficient as an electrocatalyst for HER with a lower overpotential compared to bulk MoS_2.[39] Kang *et al.* reported $NbSe_2$ nanosheets prepared by lithium-ion intercalation. The subsequent polymerization with conductive polypyrrole ($NbSe_2$@Ppy hybrid nanocomposite) enhanced the charge interaction between positively charged pyrrole and negatively charged $NbSe_2$ nanosheets, which promoted a high performance anode in lithium-ion batteries.[40]

2.2. CVD method

CVD is a well-developed bottom-up approach to grow 2D TMDCs nanosheets. Kang *et al.* (Figs. 2(a)–2(c)) put forwarded a novel CVD method to grow closely spaced MoS_2 nanosheets around 5 nm in lateral size by sulfurizing ultrahigh dense MoO_3 nanoclusters on sapphire substrate. The synthesized MoS_2 nanosheets exhibited excellent electrocatalytic properties for HER with a low onset potential of ~ 50 mV and Tafel slope of ~ 57 mV/dec.[41] Chen *et al.* reported a CVD process that gold vapor was introduced as a catalyst to guide

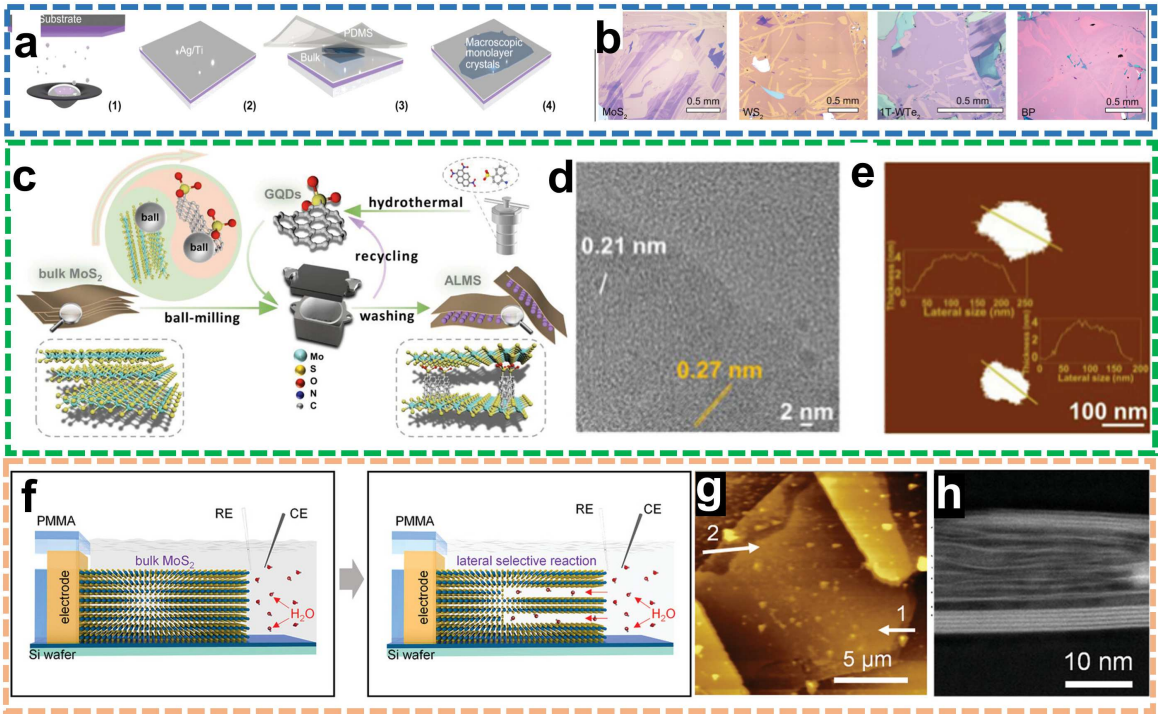


Fig. 1. Mechanically exfoliated TMDC nanosheets. (a) Schematic illustration of Ag-assisted exfoliation, and (b) optical microscope images of MoS_2, WS_2, 1T-WTe_2 and BP. (Ref. [37] Copyright 2022, Wiley-VCH). (c) Schematic diagram of ALMS synthesis and (d) their HRTEM images, and (e) AFM images with GQDs. (Ref. [38] Copyright 2023, Wiley-VCH). (f) Illustration for the preparation of MoS_2, with (g) AFM image of MoS_2 sheet, (h) TEM image of MoS_2. (Ref. [39] Copyright 2020, Wiley-VCH).

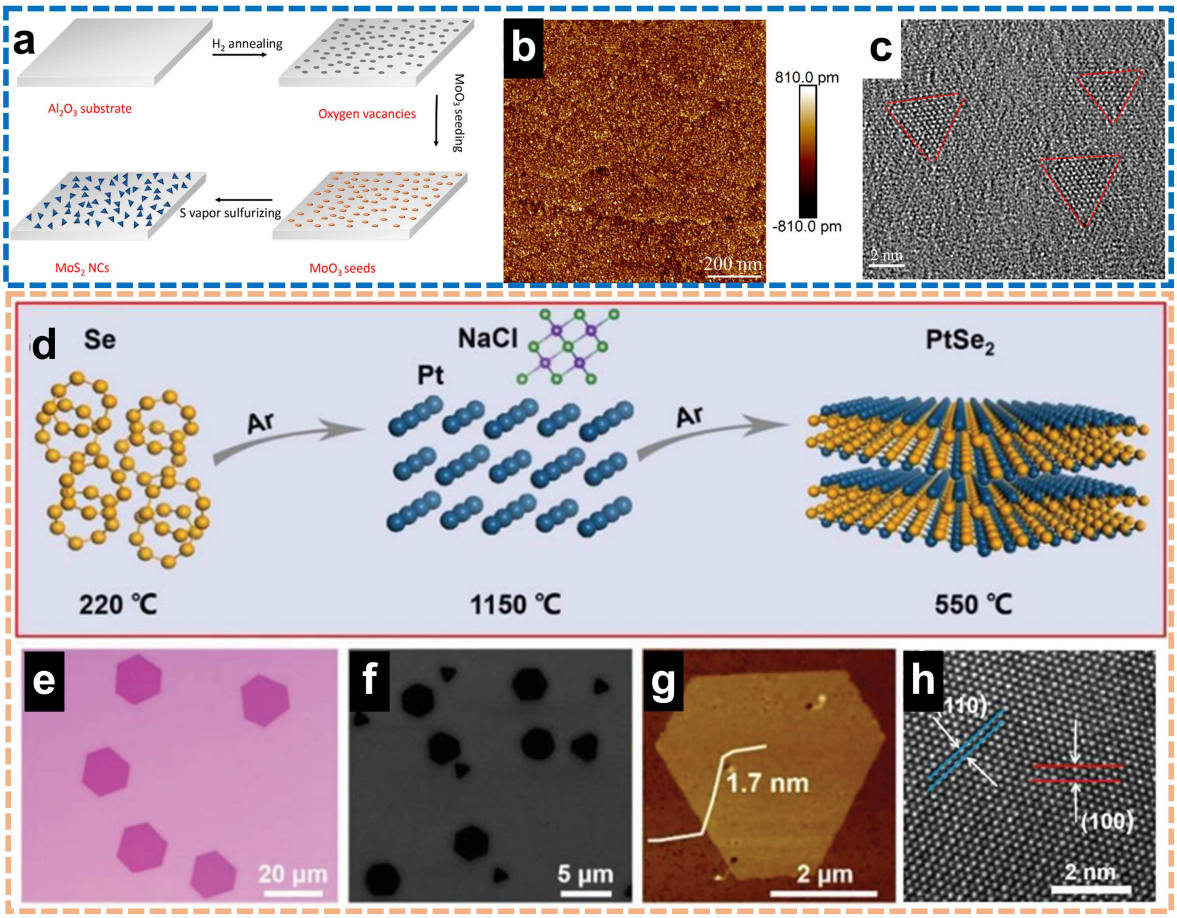


Fig. 2. The preparation of TMDCs with CVD methods. (a) Illustration of the growth process of MoS_2 nanosheets; (b) AFM image and (c) HRTEM image of the synthesized MoS_2. (Ref. [41] Copyright 2021, American Chemical Society). (d) Schematic of the preparation of $PtSe_2$; (e) optical image, (f) SEM image, (g) AFM image, and (h) atomic resolution HRTEM image of a $PtSe_2$ hexagon (Ref. [43] Copyright 2021, Wiley-VCH).

the growth and alignment of WSe_2 monolayer on *c*-plane sapphire. Highly aligned WSe_2 triangular flakes with large domain size ($>$ 130 μm), fast growth rate (4.3 μm·s^{-1}), and continuous monolayers have been successfully achieved.[42] An ambient pressure CVD route with NaCl as salt-assisted precursors was reported by Ma *et al.* (Figs. 2(e)–2(i)) to synthesize high-quality ultrathin $PtSe_2$ nanosheets on the SiO_2/Si substrate with thickness-tunable electronic and magnetoelectrical properties.[43] To reduce the high melting point of the metal and metal oxide precursors of TMDCs, Zhou *et al.* developed the molten-salt-assisted CVD and obtained a library of high quality 2D TMDCs containing 47 compounds and heterostructures, which broadened the synthesis, property studying, and potential application of TMDCs.[44]

2.3. Hydro/solvothermal method

Hydrothermal (solvothermal) synthesis is an important method to prepare materials with simple operation, low cost, and scalable production, which is favorable for the production of catalysts. Based on the hydrothermal method, a mass of TMDC catalysts have been synthesized and studied extensively, which mainly include the morphology control, crystal orientation modulation, and catalytic performance tuning. Zhang *et al.* synthesized Ni_3S_{4-x} hollow microspheres (Ni_3S_{4-x} HMs) with sulfur vacancies decorated with nanosheets by a two-step hydrothermal method, which showed excellent charging/discharging and OER performance (Figs. 3(a)–3(h)).[45] According to Chen *et al.*, *in situ* porous-sized MoS_2 nano islands were prepared by a facile one-step hydrothermal method, and the edges of MoS_2 grains were maximally exposed for efficient utilization of the active stable sites and enhancing its HER and OER performances (Figs. 3(i)–3(l)).[32] Zhang *et al.* reported a single Ru atom doped MoS_2 prepared by a one-step hydrothermal method, which exhibited excellent properties over the full pH range owe to the precise substitution of Mo atoms in the lattice of MoS_2 with Ru single atoms (Figs. 3(m)–3(r)).[46]

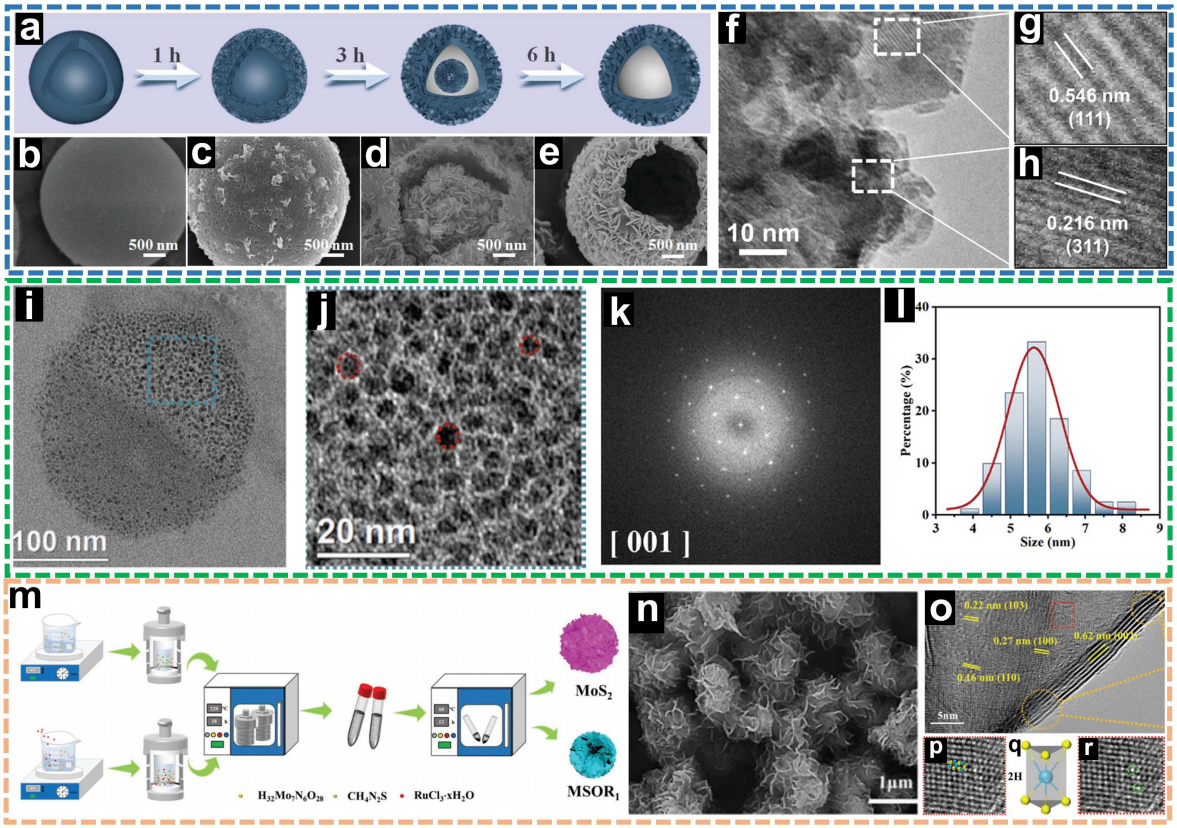


Fig. 3. Preparation of TMDCs with hydro/solvothermal methods. (a) Schematic illustration of the structural evolution during the anodic exchange process. [(b)–(e)] SEM images of samples at various stages. (f) HRTEM image of Ni_3S_{4-x} hollow microspheres with sulfur vacancies (Ni_3S_{4-x} HMs). [(g) and (h)] The enlarged view of the rectangular in panel (f). (Ref. [45] Copyright 2021, Wiley-VCH). [(i) and (j)] TEM images of porous MoS_2 nano islands. (k) FFT image of one MoS_2 nano island in panel (i). (l) Statistical map of the particle size distribution of nano island. (Ref. [32] Copyright 2023, Wiley-VCH). (m) Schematic illustration of the synthetic pathways for MoS_2 and Ru, O co-doped MoS_2 ($MSOR_1$) with different structures, and $MSOR_1$ morphology characterized by (n) SEM image, (o) TEM image, [(p) and (r)] HRTEM image, and (q) lattice arrangement of 2H phase MoS_2 (Ref. [46] Copyright 2022, Wiley-VCH).

2.4. Characterization of TMDCs

As we all know, the morphology, composition and atomic structure of the catalysts hold vital effects on their performance. Thus, a clear and accurate determination of the microstructure is essential for analyzing the structure–property relationship and promoting the development of high-

performance electrocatalysts. In this section, typical characterization methods for TMDC catalysts, using MoS_2 as an example, are introduced. X-ray diffraction (XRD) is a technique commonly used to determine the phase constitution of a catalyst. As shown in Fig. 4(a), the XRD pattern of ascorbic acid-absent (AA-absent) sample showed characteristic peaks identical to that of 2H-MoS_2 with (002) peak at 14.38°. However, the ascorbic acid-present (AA-present) sample displayed the first peak at 9.16°, confirming the formation of 1T-phase. That is, the phase constitution and structure of the 1T and 2H MoS_2 can be identified by XRD. Raman spectroscopy contains the specific fingerprint of chemical bond oscillation and thus is another viable technique for phase and bonding identification of TMDCs. A clear distinction between 2H-MoS_2 and 1T-MoS_2 has been measured in the Raman spectra of Fig. 4(b), where the 1T phase showed the characteristic peaks of J_1, J_2 and J_3 at 147 cm^{-1}, 234 cm^{-1}, 282 cm^{-1}, and 336 cm^{-1}, and the 2H phase showed the characteristic peaks of E^1_{2g} and A_{1g} at 381 cm^{-1} and 404 cm^{-1}, respectively. Meanwhile, high-resolution x-ray photoelectron spectroscopy (XPS) is capable of qualitative and quantitative measurements of the TMDCs with various allotropes or boning states. As shown in Fig. 4(c), an obvious downshift binding energy of 0.7 eV was noticed for the $3d_{5/2}$ (228.3 eV) and $3d_{3/2}$ (231.4 eV) peaks of Mo^{4+} in 1T-MoS_2. The microstructure and morphology of TMDCs can be directly clarified by scanning electron microscopy (SEM), transmission electron microscopy (TEM) and high-resolution transmission electron microscopy (HRTEM). The prepared MoS_2 nanosheets demonstrated a flower-like morphology consisting of ultra-thin nanosheets with diameters of approximately 1 μm (Fig. 4(d)). The 2H and 1T phases were further confirmed by the lattice fringes in HRTEM images in Figs. 4(e)–4(g) and 4(i)–4(k) and the corresponding fast Fourier transform (FFT) pattern in Figs. 4(h) and 4(l).[47]

In addition, high-precision characterizations from STEM can provide a comprehensive understanding of the structure and bonding state of the TMDC catalysts at atomic resolution, which will be introduced in detail in the next section.

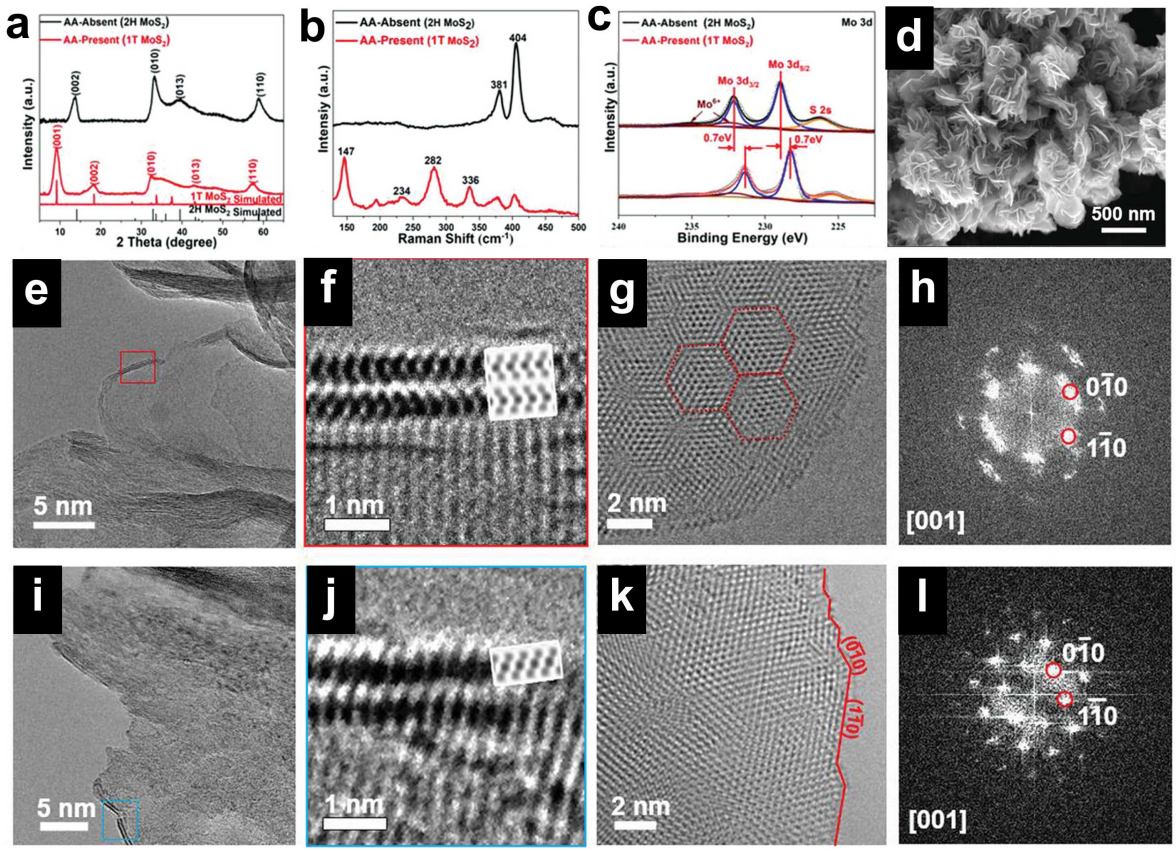


Fig. 4. Typical characterization methods of 2H-MoS_2 and 1T-MoS_2. (a) XRD patterns. (b) Raman spectra. (c) XPS spectra of Mo. (d) SEM image, (e) TEM image, (f) enlarged cross-sectional HRTEM image from indicated area in (e) with an inset of simulated HRTEM image, (g) in-plane HRTEM image, and (h) corresponding FFT pattern of 2H-MoS_2. (i) TEM image, (j) enlarged cross-sectional HRTEM image from indicated area in (i) with an inset of simulated HRTEM image, (k) in-plane HRTEM image, and (l) corresponding FFT pattern of 1T-MoS_2. (Ref. [47] Copyright 2022, Wiley-VCH).

3. Brief introduction of STEM and its application in TMDCs

Since the first construction of TEM by Ernst Ruska and his advisor Max Knoll in 1933, almost a century has passed, and sophisticated operation modes in TEM have been developed, such as the bright field imaging, dark field imaging and selected area electron diffraction (SAED) in conventional parallelly illuminated TEM, and annular dark field (ADF) imag-

ing, annular bright field (ABF) imaging, convergent beam electron diffraction (CBED) and ptychography in convergently illuminated STEM. Especially, with the great contribution of Stephen J. Pennycook, STEM-EELS with atomic resolution imaging and elemental recognition have received increasing concerns and become a comprehensive platform for the research of materials science. The booming development of TMDCs is also promoted energetically by advanced TEM and STEM, with the establishment of *Z*-contrast imaging technique and the corresponding incoherent imaging theory.

3.1. Development of STEM and its operation modes

The STEM is mainly promoted by Stephen J. Pennycook since 1980s, the founder of *Z*-contrast imaging and a pioneer of STEM and EELS today. As shown in Fig. 5, the STEM is illuminated with a focused electron probe to scan across the specimen in a 2D raster. Annular detectors with various radii collect electrons scattered by the specimen with different collection semi-angles (β), and form ADF and ABF images. By the principle of reciprocity in STEM imaging, the ADF detector is equivalent to using a large incoherent illuminating source in a conventional HRTEM,[48] which forms incoherent image with improved resolution. Especially, high angle ADF (HAADF) image collects the Rutherford scattering electrons from the nuclei in the specimen with a rather larger collection angle ($>$ 50 mrad), and thus shows an approximate Z^2 dependence contrast, which is also named *Z*-contrast image (*Z* is the element number). Meanwhile, simultaneous elemental analysis can be achieved with x-ray energy dispersive spectroscopy (EDS) equipped above the specimen or electron energy-loss spectroscopy (EELS) under the specimen (Fig. 5).[49]

By 1979, Pennycook and his fellow had obtained the first HAADF images of catalyst particles.[50] The methodology of *Z*-contrast imaging was then developed in the next decade and atomic resolution was achieved.[51] Working with Nigel Browning and Matthew Chisholm, Pennycook also went on to show that EELS could be used alongside ADF imaging to obtain chemical information.[52] Since the early 2000s, working with Nellist, Krivanek, and Dellby, Pennycook's group in ORNL started their attempt of spherical aberration correction for the electron probe of STEM, and the first sub-angstrom imaging of a crystal lattice, as well as the first spectroscopic identification of a single atom within a bulk crystal was achieved.[53,54] Till 2010, the breakthrough results of Pennycook's group on atom-by-atom imaging of boron, carbon, nitrogen and oxygen were realized, which was highlighted on the cover of *Nature*.[55,56] Now the spherical aberration corrected STEM can reach an atom-by-atom imaging and chemical analysis with the resolution smaller than 0.5 Å.[57]

3.2. Atomic structure analysis of TMDCs via STEM

As discussed above, due to different receiving angles, one or several signals can be collected at the same time during the experiment to obtain different images and chemical information of materials at the same position simultaneously, which turns the STEM into a powerful tool for the atomic structure analysis of TMDCs. The STEM images often contain morphology and structural information of TMDCs, while the EDS and EELS can review composition information during imaging. What is more, the EELS obtained by collecting electrons from the inner hole of the annular detector can resolve chemical bonding states of elements in the specimen.

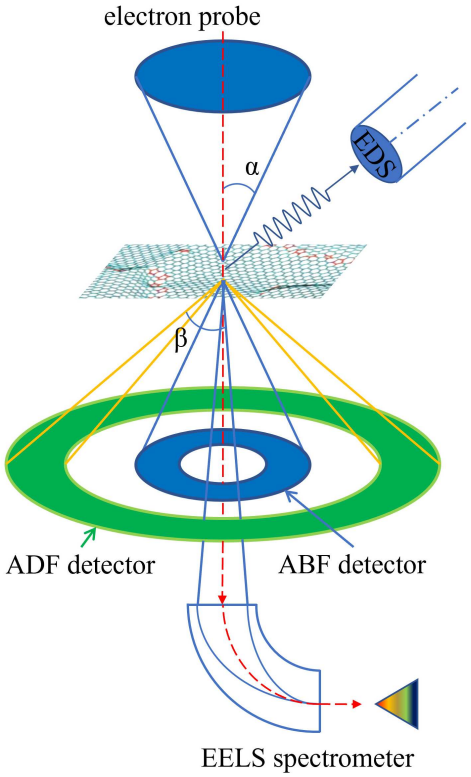


Fig. 5. Schematic diagram of the common imaging and spectrum modes in a STEM, composed of ADF or ABF images, EDS, and EELS (Ref. [57] Copyright 2021, Elsevier).

3.2.1. HAADF-STEM imaging

In an atomic resolution HAADF-STEM image, positions of atoms are recorded straightforwardly, and thus the crystal structure can be resolved.[44] Elements on a certain position can be determined as well by their intensities, i.e., the brightness of the atoms in the image, since the intensity of an atomic image is proportional to Z^2. Ge *et al.* reported an optimized electrocatalyst of MoS_2 with abundant Mo vacancy and NiCoP clusters. As shown in Figs. 6(a) and 6(b), the atomic structure of 2H-MoS_2 nanosheet with Mo vacancies was clearly identified with the atomic resolution HAADF-STEM imaging, where the positions of Mo vacancies were determined accurately along the line profiles of Mo atomic rows.[58] As shown in Figs. 6(c)–6(e), Shao *et al.* proposed Pt and Ru heteroatom doped 2D MoS_2 nanosheets for a boosted HER electrocatalyst, with atomic structure accurately determined by HAADF-STEM imaging. The intensity of atoms in the HAADF images revealed clearly the perfect hexagonal MoS_2 (Fig. 6(c)),

the Mo vacancies in MoS_2 (yellow circles in Fig. 6(d)), Pt (blue circles in Fig. 6(e)) and Ru (green circles in Fig. 6(e)) substitutions.[59] Ji *et al.* investigated the interlayer coupling dependent lithium intercalation induced phase transition in bilayer MoS_2 (BL-MoS_2) using ADF-STEM imaging. The 2H phase and 1T′ phase of MoS_2 in the BL-MoS_2 were clearly identified with the atomic resolution ADF image and the corresponding FFT patterns (Fig. 6(f)).[60] Zhang *et al.* designed a vdW heterojunction of MoS_2/WSe_2 bilayers with a periodically variable local bandgap, which is modulated by the lattice mismatch of the hetero-bilayers. The periodic variation in local interlayer atomic registry of the hetero-bilayers exhibited a well-defined Moiré pattern, which was observed by scanning tunneling microscopy (STM) and STEM (Figs. 6(g)–6(j)). The STM images in Figs. 6(g) and 6(h) displayed the Moiré pattern of monolayer (ML) MoS_2 on ML-WSe_2 with a lattice constant of 8.7 ± 0.2 nm, while the STEM image in Figs. 6(i) and 6(j) depicted the Moiré pattern with atomic resolution, which displayed the various atomic alignments for AA, AB_{Se}, bridge (Br), and AB_W stacking (the symbol of AB_{Se} (AB_W) means that the hexagonal lattices of the metal atoms in the two MLs are stacked in an AB manner, with the Se (W) atoms in the bottom ML not covered by any atoms in the upper ML). Electron diffractions, both the conventional SAED and CBED, reflect the arrangement of atoms in reciprocal space, and thus can be used to determine the phase of materials, such as the example in Fig. 6(f). Beside the crystallographic information in reciprocal space, CBED patterns can be used to reconstruct complex-amplitude distributions of the probe and the specimen, and thus the real-space image, i.e., ptychography. Recently, the Moiré pattern of twisted bilayer WSe_2 resolved by ptychography has achieved a resolution of 0.44 Å without an aberration corrector, which promotes a major step toward broadening the applications of electron microscopy.[61]

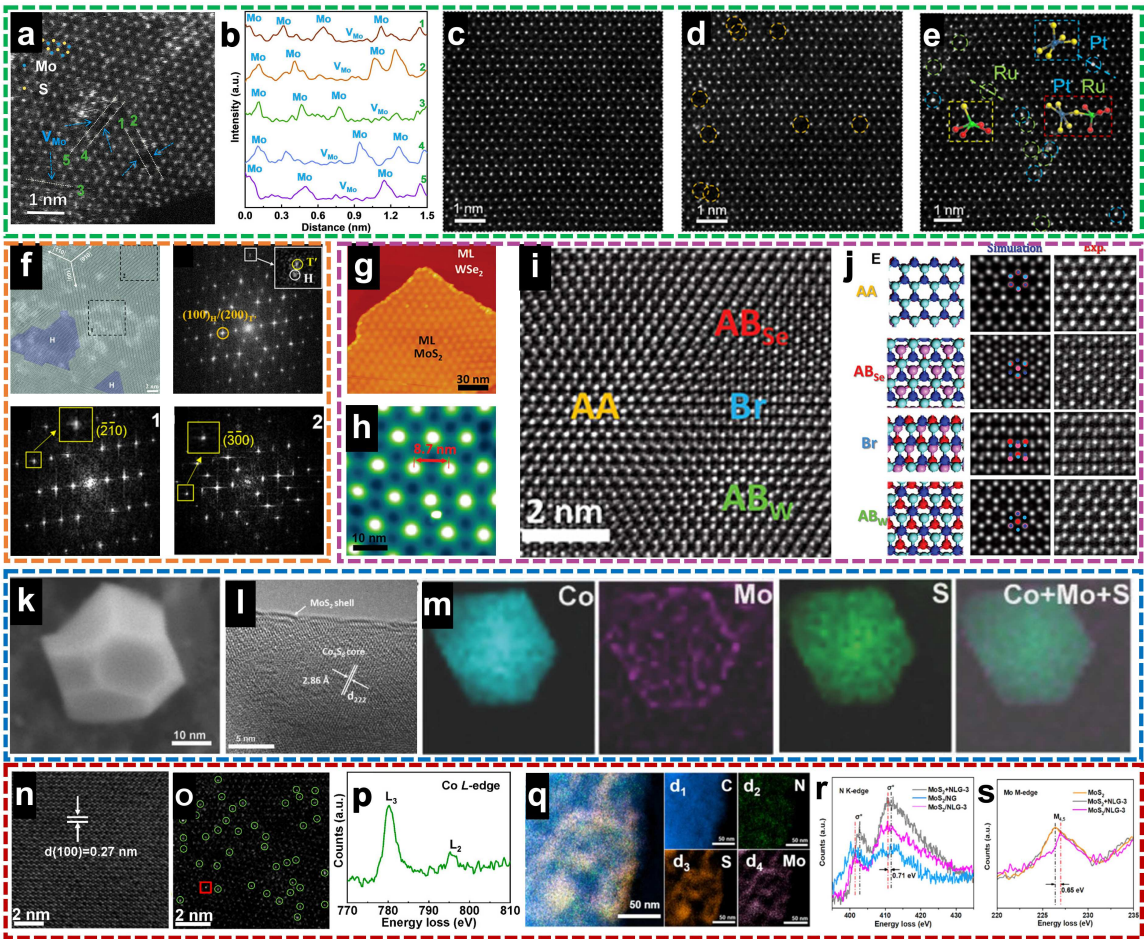


Fig. 6. Atomic structure characterization of TMDCs via the advanced analytical STEM. (a) HAADF-STEM image of MoS_2, with (b) the intensity profiles extracted from atomic rows in panel (a). (Ref. [58] Copyright 2022, American Chemical Society). HAADF images of (c) pure MoS_2, (d) MoS_2 with Mo vacancies, and (e) MoS_2 with Pt and Ru substitutions. (Ref. [59] Copyright 2021, Wiley-VCH). (f) An atomic resolution ADF-STEM image showing lithiated bilayer MoS_2 and the corresponding FFT image. (Ref. [60] Copyright 2021, American Chemical Society). (g) STM image for a MoS_2/WSe_2 vdW heterostructure on the highly oriented pyrolytic-graphite substrate. (h) Close-up STM image showing the hexagonal Moiré pattern with a periodicity of 8.7 nm. (i) Atomically resolved STEM image of the Moiré pattern with typical regions of AA, AB_{Se}, Br, and AB_W stacking. The atomic model, simulated image and experimental STEM image of each region shown in (j) depicted its variation of atomic registry. (Ref. [61] Copyright 2017, American Association for the Advancement of Science). (k) SEM image, (l) TEM image and (m) EDS element mapping of Co_9S_8/ML MoS_2. (Ref. [62] Copyright 2018, Wiley-VCH). (n) HAADF-STEM image of monolayer MoS_2. (o) HAADF-STEM image of Co@MoS_2. (p) EELS obtained from the red rectangle in panel (l). (Ref. [63] Copyright 2022, American Chemical Society). (q) Energy filtered TEM image of MoS_2/NLG-3 catalysts, with [(r) and (s)] N *K*-edge and Mo *M*-edge EELS spectra of MoS_2, MoS_2/NG, MoS_2 + NLG-3, and MoS_2/NLG-3. (Ref. [64] Copyright 2021, American Chemical Society).

3.2.2. STEM-EDS analysis for elemental distribution

It is of great significance to determine the element distribution of catalysts for the research of structure–activity relationship. The bright and focused electron probes in STEM mode can excite characteristic x-rays of every element in the sample and thus produce the EDS mapping up to atomic resolution. Li *et al.* demonstrated a conceptual strategy of precisely tuning tensile surface strain on Co_9S_8/MoS_2 core/shell nanocrystals for boosting the hydrogen evolution reaction (HER) activity by controlling the MoS_2 shell numbers. SEM and TEM images in Figs. 6(k) and 6(l) showed that the Co_9S_8 core was confined in monolayer MoS_2. What is more, the EDS mapping demonstrated clearly that Co was mainly concentrated in the central region of the nanocrystal, while Mo was significantly distributed along its periphery despite being present throughout the nanocrystal (Fig. 6(m)). Therefore, it can be inferred that Co_9S_8/MoS_2 possessed the core–shell structure with Co_9S_8 in the inner layer and MoS_2 in the outer layer.[62]

3.2.3. STEM-EELS analysis for chemical bonding

When the electron beam passes through the sample, some incident electrons undergo inelastic collision with the atoms in the sample, and cause atoms ionization in the sample, valence band electron excitation, valence band electron oscillation, electron–phonon interaction, and so on, which result in an energy loss of the electron beam. By collecting these inelastic scattered electrons, EELS can be obtained, and the chemical composition, electronic structure, and chemical bonding information of the sample can be resolved. Gong *et al.* reported a single atomic catalyst, Co@MoS_2, for improved OER performance, in which Co single atom anchored on top of Mo atom was corroborated by STEM and EELS analyses (Figs. 6(n)–6(p)).[63] Meanwhile, EELS as an efficient synthetic tool to resolve chemical bonding information of the sample plays a vital role in explaining catalytic mechanisms. As shown in Fig. 6(q), Qin *et al.* designed a pH-universal HER catalyst by *in situ* growing 2H-MoS_2 nanosheets on N-doped, laser-induced mesoporous graphene (MoS_2/NLG). Energy filtered TEM images (Fig. 6(q)) indicated the formation of MoS_2 and successful nitrogen doping on graphene. Meanwhile, the shift of the characteristic EELS peaks of N and Mo in Figs. 6(r) and 6(s) indicated the formation of Mo–N coordination at the interface, which can improve the HER catalytic activity of marginal Mo atoms in basic electrolytes.[64]

4. TMDCs electrocatalysts for hydrogen energy conversions and active site identification via STEM

Benefiting from their unique structures, such as controlled phase transition, abundant active sites of vacancies and substitutional atoms, and tunable band structure caused by lattice strain, TMDCs have been developed as novel HER electrocatalysts. Along with the synergetic effects from heterojunctions, TMDCs based catalysts also have excellent OER and ORR performance. Thus, TMDCs have been extensively studied as promising catalysts used in hydrogen energy conversions. In comparison with conventional precious metal materials, TMDCs exhibit comparable activities but much better economy. The key issue of catalyst design is the identification of the atomic structure of the active sites, which can be achieved by the advanced atomic resolution STEM. The kinetic processes of OER, HER, and ORR have been well summarized in the previous reviews.[12,27] However, the configuration and evolution of the correlative active sites are still controversial. Therefore, a thorough resolution of the active sites with atomic precision is crucial for explaining the catalytic mechanisms and providing theoretical guidance for the synthesis of high-performance catalysts, and thus prompting the development of hydrogen energy conversions. Accordingly, the electrocatalysis properties of TMDCs in recent years are enumerated in Table 1. Internal mechanisms of the electrocatalytic reactions along with the active site identifications via STEM are summarized in this section.

4.1. Highly active phase

The phase transition of TMDCs can modulate their band structures and thus the charge transfer, which will significantly affect the intrinsic electrocatalysis activity. The key to the synthesis of highly active phase of TMDCs lies in the formation of specific thermodynamically metastable structures that exist in a temporarily higher energy state and an eventual transition to a lower energy configuration. For example, Liu *et al.* established an efficient colloidal chemical strategy for the controlled synthesis of metallic 1T′ phase dominated WS_2 nanostructures, which exhibited higher HER activity in H_2SO_4 electrolyte than that of 2H-WS_2, The STEM image revealed the successful synthesis of 1T′ phase, which promoted the progress of electrocatalytic reaction.[81] Shi *et al.* reported a simple CVD method to synthesize atomically thin 1T-$PtSe_2$ on Au foil as an electrode in HER (Figs. 7(a)–7(c)). Furthermore, large-scale STM and STEM images showed the covering of 1 ML 1T-$PtSe_2$ on Au terraces, and the phase and atomic structure of various point defects in ML 1T-$PtSe_2$ have been resolved by STEM, which proved the high quality ML 1T-$PtSe_2$ with abundant point defects on Au foils brought about its excellent electrochemical properties.[67] Han *et al.* reported high purity 1T-WS_2 monolayers with single atom V (V SACs@1T-WS_2) prepared via a one-step CVD method and applied in high efficiency HER (Figs. 7(d)–7(g)). The STEM image, together with Raman spectroscopy, confirmed the atomic dispersion of V species on the 1T-WS_2 monolayer. Under the coordinated action of V single atom and highly active 1T-WS_2, the V SACs@1T-WS_2 showed improved HER performance with a low overpotential of 185 mV at a current density of 10 mA/cm^2 and a small Tafel slope of 61 mV/dec.[82]

Table 1. Summary of electrocatalysis performances of TMDCs for water electrolysis in recent five years.

Catalyst	Electrocatalysis performances				Year
	Reaction	Electrolyte	Overpotential/$E_{1/2}$ (η vs. RHE)	Tafel slope (mV·dec^{-1})	
MoS_2	HER	0.5 M H_2SO_4	76 mV @10 mA·cm^{-2}	47.4	2018[65]
WS_2	HER	0.5 M H_2SO_4	222 mV @6 mA·cm^{-2}	97	2019[66]
$PtSe_2$	HER	0.5 M H_2SO_4	210 mV @10 mA·cm^{-2}	38	2019[67]
$MoSe_2$	HER	0.5 M H_2SO_4	73 mV @10 mA·cm^{-2}	51	2020[68]
WS_2	HER	1.0 M KOH	109 mV @10 mA·cm^{-2}	74	2021[69]
$CoSe_2$	HER	1.0 M KOH	98 mV @10 mA·cm^{-2}	63.4	2021[70]
$PtSe_2$	HER	0.5 M H_2SO_4	11 mV @10 mA·cm^{-2}	48	2021[71]
VSe_2	HER	0.5 M H_2SO_4 1.0 M KOH 1.0 M PBS	67.2 mV @10 mA·cm^{-2} 72.3 mV @10 mA·cm^{-2} 122.3 mV @10 mA·cm^{-2}	51 71 66	2022[72]
MoS_2	HER	0.5 M H_2SO_4	171 mV @10 mA·cm^{-2}	122	2023[73]
$MoSe_2$	HER	1.0 M KOH	119 mV @10 mA·cm^{-2}	89	2023[74]
NbS_2	HER	0.5 M H_2SO_4	55 mV @10 mA·cm^{-2}	36.25	2023[75]
WS_2	HER OER	1.0 M KOH	274 mV @10 mA·cm^{-2} 1.535 V @10 mA·cm^{-2}	107 92	2021[76]
2M-MoS_2	HER OER	1.0 M KOH	31 mV@50 mA·cm^{-2} 170 mV @50 mA·cm^{-2}	43.2 38.9	2022[77]
$PtSe_2$	HER OER	1.0 M KOH	59 mV @10 mA·cm^{-2} 310 mV @10 mA·cm^{-2}	88 129.3	2022[78]
(Fe, Co)Se_2	OER ORR	0.1 M KOH	266 mV @10 mA·cm^{-2} 0.89 V	56.3 46.5	2023[79]
MoS_2	ORR	0.1 M KOH	0.88 V	26	2022[80]

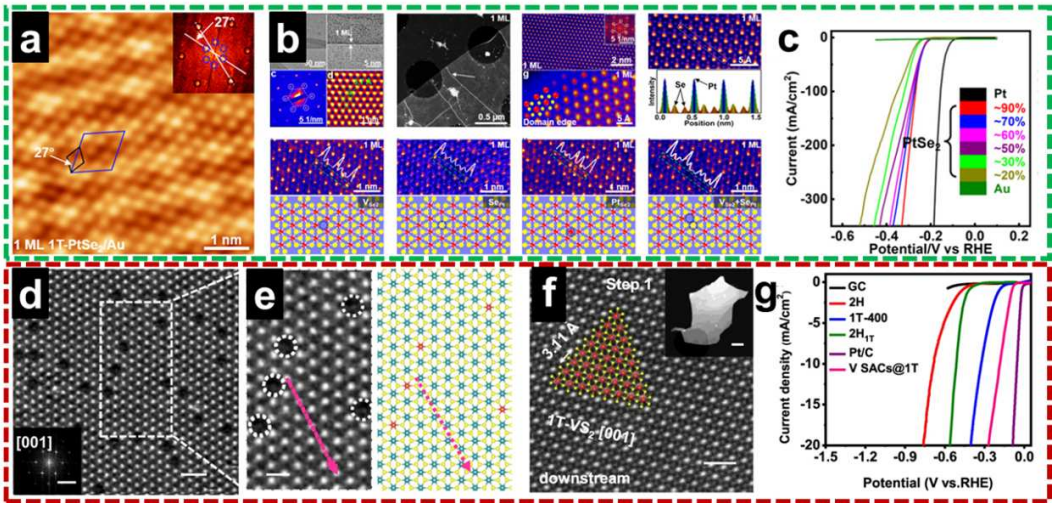


Fig. 7. Phase identification via STEM for TMDCs electrocatalysts. (a) Atomic resolution STM image of ML 1T-$PtSe_2$ on Au foils showing the Moiré patterns. (b) TEM and atomic resolution HAADF-STEM showing the phase and atomic structure of various point defects in ML 1T-$PtSe_2$. (c) HER performance of $PtSe_2$. (Ref. [67] Copyright 2020, American Chemical Society). [(d) and (e)] HAADF-STEM image of single V and (f) a 1T-VS_2 domain in 1T-WS_2. (g) Electrochemical performances of the synthesized catalysts. (Ref. [82] Copyright 2019, Springer Nature).

4.2. Heteroatom doping

Heteroatom doping (includes nonmetallic and metal element doping) of TMDCs is another effective way to obtain high performance electrocatalysts. In general, the external atom can replace or combine with the original atom, which can not only regulate the electronic structure of the neighboring atom to obtain better hydrogen binding energy and electrical conductivity, but also serve as a new active site to improve the constitutive activity by enhancing the electron density of state perpendicular to the basal plane of TMDCs. According to Zhang *et al.*, large-area uniform Nb-WS_2 monolayers with high concentration of Nb doping were developed by salt-assisted CVD processes, which generated a significantly improved HER catalytic performance compared to pristine WS_2 nanosheets. As shown in Figs. 8(a) and 8(b), the active site was proved to be the successful Nb substitution of W in the

WS_2 monolayer by STEM.[66] Zheng *et al.* successfully prepared a MoS_2 nanofoam catalyst with co-confining selenium on surface and cobalt in inner layer. STEM images (Figs. 8(c)–8(e)) verified that the excellent catalytic activity for HER with long-term stability and high current density had been achieved by the precise doping of Se on the surface and Co in the inner layer of the MoS_2.[83] Zhang *et al.* presented a Ru doped MoS_2 synthesized by a simple one-step impregnation method. As shown in Figs. 8(f)–8(h), HAADF-STEM results showed that single Ru atom was successfully doped into MoS_2, which confirmed Ru doping effectively regulated the intrinsic electronic structure of inert 2D MoS_2 with structural phase stability and thus enhanced its alkaline HER activity. The author also claimed that the Ru doping can induce the transition of MoS_2 from 2H to 1T phase, and the generation of S vacancies, which prompted the HER performance of the catalyst.[84]

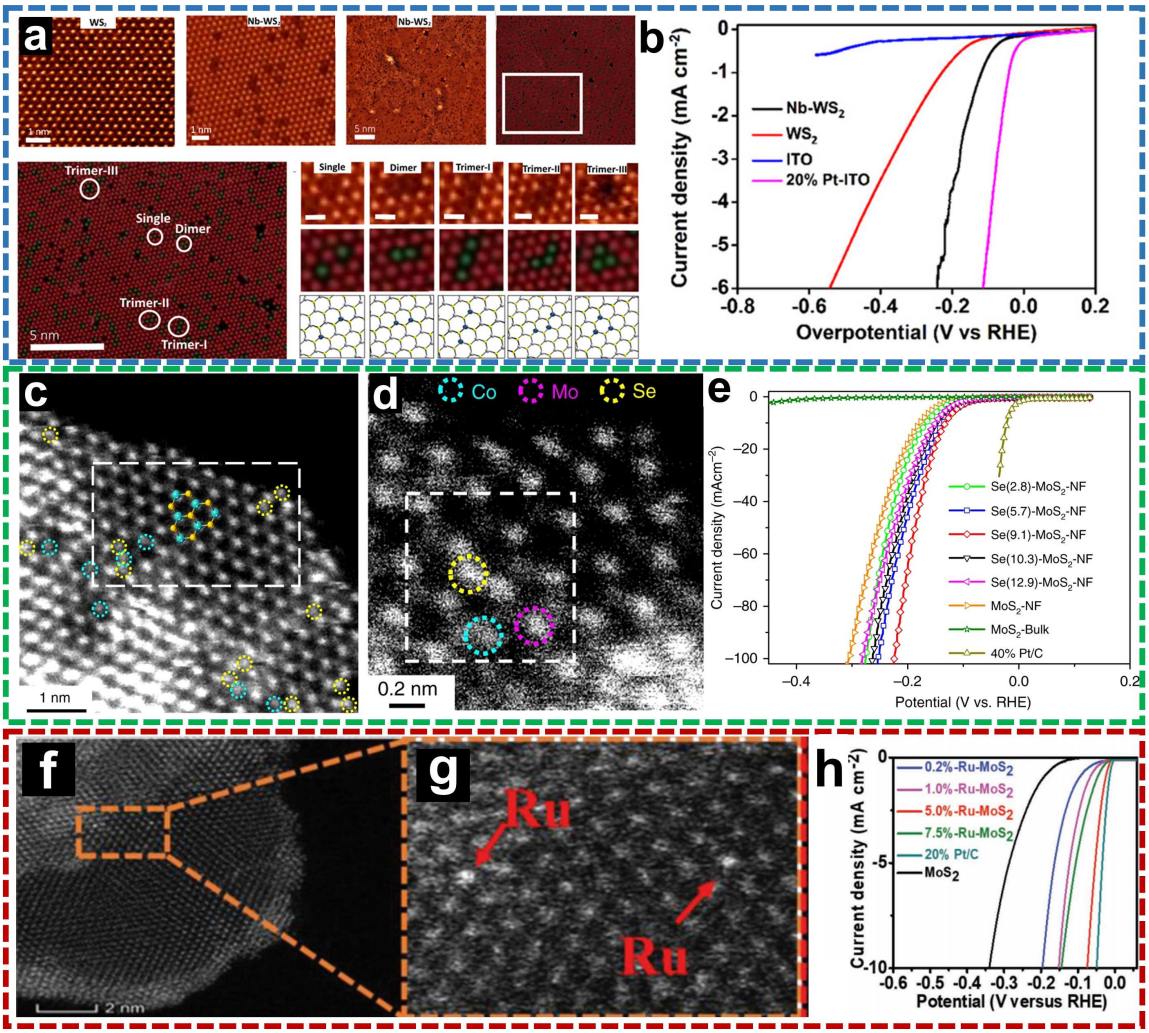


Fig. 8. Doped hetero atoms identified via STEM in TMDCs electrocatalysts. (a) Atomic resolution STEM image of Nb-WS_2, with clearly resolved Nb substitutions of single, dimer, and trimer-I, trimer-II, trimer-III. (white, W sites; green, Nb site; black hole, metal vacancy). (b) LSV curve of Nb-WS_2 and the control samples. (Ref. [66] Copyright 2020, American Chemical Society). (c) Low pass filtered large area atomic-resolution HAADF-STEM image of the Co/Se-MoS_2-NF. (d) Atomic-resolution HAADF-STEM image of the Co/Se-MoS_2-NF. (e) Electrochemical performance of Co/Se-MoS_2-NF. (Ref. [83] Copyright 2020, Springer Nature). [(f) and (g)] Atomic resolution HAADF image of Co/Se-MoS_2-NF. (h) Polarization curves of Co/Se-MoS_2-NF with different Ru contents. (Ref. [84] Copyright 2019, Wiley-VCH).

4.3. Vacancy

Vacancy, a widespread defect in crystals refers to the free space points in the lattice, is another kind of point defect. In addition to regulating the band structure and carrier migration characteristics, the introduction of vacancies can change the electron distribution, and then affect the absorption process of reactive molecules, thus improve the efficiency of catalysis. According to Yang *et al.*, individual sulfur vacancies were controllably introduced by a helium ion microscope onto a ML MoS_2, and directly observed via atomic resolution STEM (Figs. 9(a)–9(d)). The atomically resolved vacancies with accurate density and local strain were directly correlated to the superior HER performance of the defective MoS_2 with a smaller Tafel slope (44 mV·dec^{-1}) and a lower overpotential (230 mV @ 10 mA·cm^{-2}).[85] Ping *et al.* presented a defective $PtSe_2$ with various vacancy densities introduced by a mild Ar plasma treatment. The STEM images in Figs. 9(e)–9(h) revealed Pt_{Se} antisite, Pt cluster, and

the vacancies of V_{Se} and V_{Pt} quantitatively, which explained the improved HER properties of the defective $PtSe_2$ with a smaller Tafel slope (48 mV·dec^{-1}) and a lower overpotential (11 mV @ 10 mA·cm^{-2}).[71] Zhou *et al.* designed a ReS_2 film with Re vacancies ($V_{Re}ReS_2$) by KI-assisted CVD approach (Figs. 9(i)–9(k)). The atomic resolution STEM image and the inset FFT revealed clearly the 1T′ ReS_2 with omnipresent Re vacancies. It can be concluded that the improved HER properties of $V_{Re}ReS_2$ in Fig. 9(k) arose from the V_{Re} induced Re–Re bonds, which could accept extra electrons from active S sites to weaken the S−H adsorption strength, and thus leading to more facile kinetics for HER.[86]

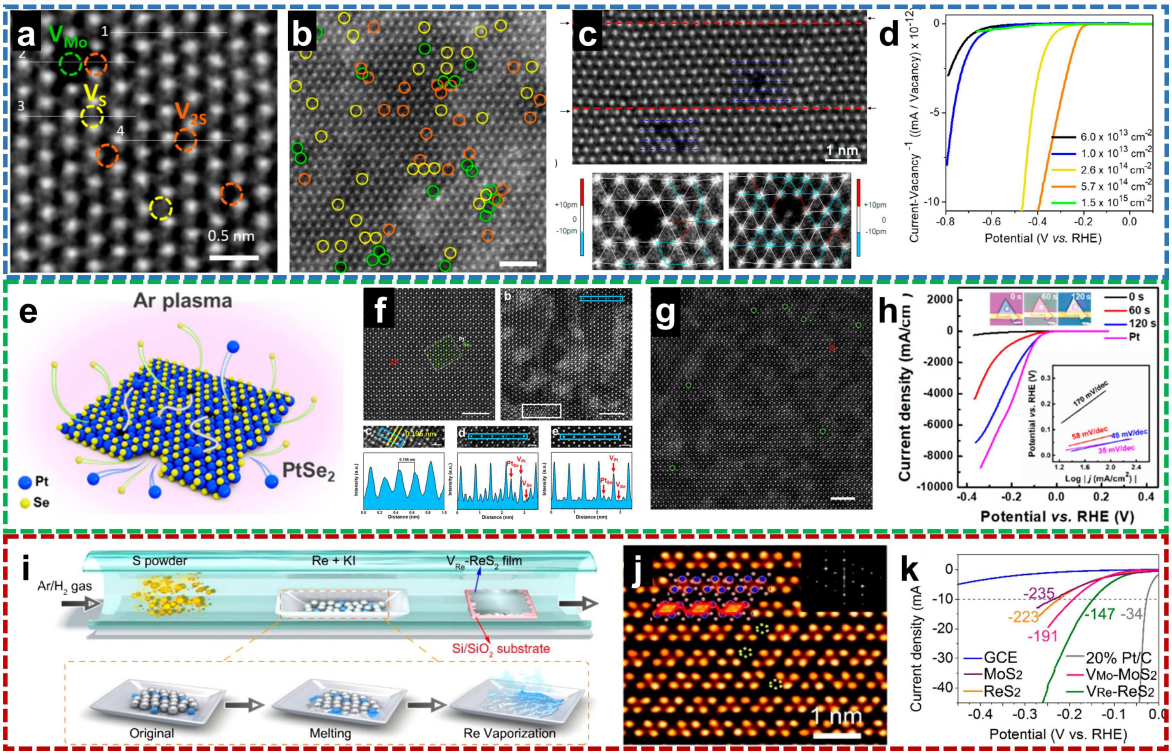


Fig. 9. Vacancy identification via STEM for TMDCs electrocatalysts. [(a) and (b)] HAADF-STEM images of a single layer MoS_2 with single S vacancy (yellow circles, V_s), double S vacancy (orange circles, V_{2s}), and single Mo vacancy (green circle, V_{Mo}). (c) HAADF-STEM observations of local strain and atomic structure in single layer MoS_2. (d) HER performance of MoS_2 with various vacancy densities. (Ref. [85] Copyright 2019, American Chemical Society). (e) Schematics for the Ar plasma treatment of $PtSe_2$. [(f) and (g)] HAADF-STEM images of a pristine $PtSe_2$, and Ar plasma treated $PtSe_2$ with point defects of Pt_{Se}, V_{Se} (green circles), and V_{Pt} (red circles). Scale bar is 2 nm. (h) LSV curves of catalysts. (Ref. [71] Copyright 2021, American Chemical Society). (i) Illustration of the preparation, and (j) HAADF-STEM image of V_{Re}–ReS_2, with Re vacancies highlighted in yellow circles. (k) Polarization curves of catalysts. (Ref. [86] Copyright 2018, American Chemical Society).

4.4. Heterogeneous interface

Due to the strong coupling interaction between the different components and the resulting interface, the heterostructure can theoretically be used as a transport channel for the electronic or electrocatalytic reaction intermediates between the different components, which not only helps to improve the activity and stability of the electrocatalytic process, but also combine active sites with multiple catalytic functions. Thus, the study on interface structures of heterojunctions plays a key role in the designing of novel TMDCs based electrocatalysts with versatile performances.

Tan *et al.* designed MoO_2/MoS_2 heterostructures by tuning the gap distance between the growth substrate and the metal precursors. The morphology of the heterostructure was characterized by AFM, and the atomic structure of the interface between the atomically thin MoO_2 and MoS_2 in the heterostructure was resolved by STEM, which demonstrated the heterogeneous interfaces contributed to the excellent HER performance.[87] Zheng *et al.* constructed a bifunctional oxygen electrocatalyst (Fe, Co)Se_2@Fe_1/NC containing heterogeneous interfaces of Fe_1/NC and (Fe, Co)Se_2. As shown in Fig. 10(d), the heterointerface between Fe_1/NC and $FeSe_2$ as well as that between $FeSe_2$ and $CoSe_2$ were resolved with atomic resolution STEM and EDS, which confirmed that the heterojunctions accelerated electron transfer, provided milder adsorption sites, and thus enhanced the OER performance of (Fe, Co)Se_2. The LSV curves demonstrated that (Fe, Co)Se_2 outperformed the benchmark catalysts of $Pt/C + RuO_2$ in alkaline media.[79] Alternatively, Wu *et al.* realized a novel heterostructure based on Ni_3N nanoparticles growing on vertically stacked 1T′-MoS_2 monolayers (Ni_3N@2M–MoS_2) The heterogeneous interfaces between Ni_3N and MoS_2 resolved by atomic resolution HRTEM and STEM in Figs. 10(f) and 10(g) confirmed the superior OER performance with a large current density of 1000 mA·cm^{-2} (Fig. 10(h)) originated from the heterointerface.[77]

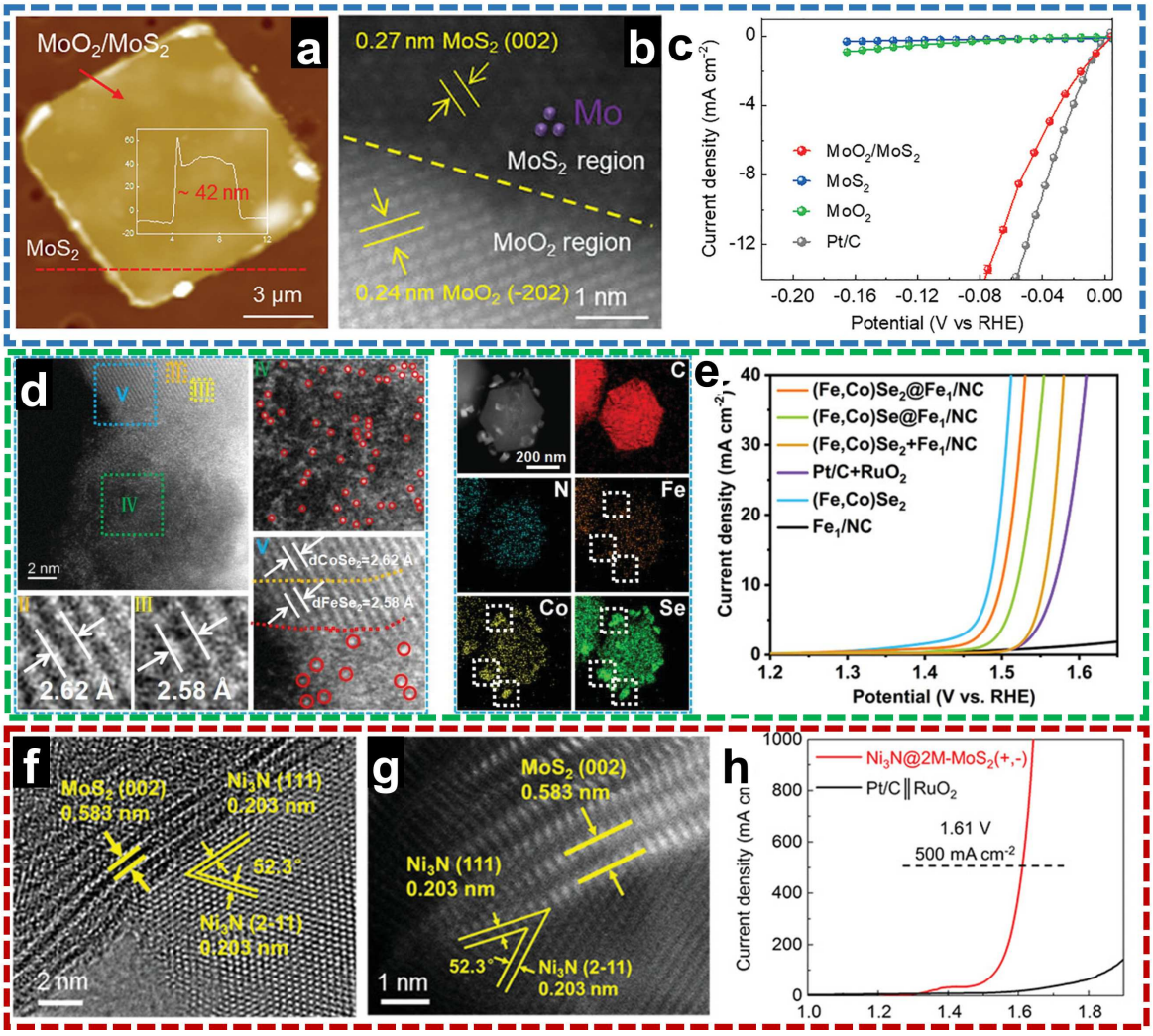


Fig. 10. Heterointerface identification via STEM in TMDCs electrocatalysts. (a) and (b) AFM, HAADF-STEM images of the MoO_2/MoS_2 heterojunctions. (c) LSV curves of the MoO_2/MoS_2 nanostructures. (Ref. [87] Copyright 2021, Wiley-VCH). (d) HAADF-STEM images and EDS mapping of (Fe, Co)Se_2@Fe_1/NC. (e) OER performance of (Fe, Co)Se_2@Fe_1/NC and the control samples. (Ref. [79] Copyright 2023, Wiley-VCH). (f) HRTEM image, (g) HAADF-STEM image, and (h) overall water splitting performance of Ni_3N@2M-MoS_2. (Ref. [77] Copyright 2022, Wiley-VCH).

4.5. Strain

Strain is usually aroused by the change of lattice constant in TMDCs, and includes internal strain and externally applied strain. The external strain is introduced by external forces, such as bending, twisting, folding, etc., applied on 2D materials, and the internal strain is caused by alloying, doping, phase transition, and forming of heterostructures during the growth. Thus, it is common in 2D materials, and can be used to tune the electrocatalysis properties of TMDCs. Gao *et al.* reported an efficient HER electrocatalyst constructed with magnetron sputtering Co, Ni co-doped $MoTe_2$ flakes. The HAADF-STEM images showed that the $MoTe_2$ in the nanofilm transformed from 2H phase to 1T′ phase with the increase of doping concentration. Geometric phase analysis (GPA) was launched based on the atomic resolution STEM images, and the strain distribution on the nanofilms was resolved. The STEM results indicated that the strain and charge injection caused by doping induced the phase transformation of $MoTe_2$ nanofilms, and thus enhanced its HER activity.[88]

In summary, the various phases, point defects, heterojunctions and strain are ubiquitous in TMDCs, and taking advantage of them properly can help to adjust the electronic structure of the active sites and the adsorption energy of the TMDCs based electrocatalysts. Thus, phase engineering, defect engineering, interface engineering and strain engineering can be applied to the development of novel TMDCs electrocatalysts with high efficiency, multifunction and good economy.

5. *In situ* STEM for electrocatalysis

Although traditional TEM is a powerful tool for observing the atomic structures of materials, and has played an undisputed role in promoting the development of materials science, it performs static characterization of materials in a vacuum environment, while the properties and behaviors of many materials may change under actual working conditions. *In situ* TEM provides conditions close to the real environment, and more

directly relates the microstructure evolutions of materials with respect to external stimulations and environmental changes. Thus, it is of great significance for expanding the TEM observations for materials to track and understand the nature of various dynamic progress during reactions or loading conditions, which will provide solid evidence for the designing and preparing of materials with novel properties.

5.1. Development of *in situ* STEM

Over the past two decades, the application of TEM and STEM has evolved from nanoscale research methods to dynamic techniques to measure and understand the effects of environmental conditions on nanoscale morphology, structure, chemistry, and properties of materials. The *in situ* TEM and STEM study started from the effects of electron beam redaction on the nanomaterials. For example, sub-nanometer semiconducting nanoribbons were fabricated from ML MoS_2 by *in situ* electron irradiation,[89] and the focused electron beam was used to tailor nanowires on ML TMDCs with metallicity.[90] However, introducing the external stimulus along with gas or liquid environmental conditions without the loss of resolution remains great challenge.

At present, a variety of sample holders with micro-electro mechanical system (MEMS) chips were developed to permit multiple catalytic environments of liquids or gaseous with stimuli such as heating, cooling, straining, laser, electricity etc., and precise control can be achieved in the catalytic process. The speed and fidelity of data recording devices have also greatly improved over the past few decades, from charge-coupled device (CCD) to modern direct electron detectors capable of recording at frame rate in excess of 1 kHz. With the development of *in situ* technology, reproducing the process of catalytic reaction with accurate measurements of stimulus parameters, material structures and properties, and confirming the structure–activity relationship of catalyst dynamically can be achieved and become the current research hotspot.

5.2. Application of *in situ* STEM in TMDCs electrocatalysts

In situ electron microscopy has a guiding significance for the understanding of the growth mechanics of 2D materials and the active site identification in the catalytic reaction process. Ryu *et al.* reported a temperature-driven $PtSe_2$ phase transition under an *in situ* heating STEM. Atomic resolution STEM images in Figs. 11(a)–11(l) showed clearly that the layered 1T-$PtSe_2$ transformed into 2D ultra-thin nonlayered PtSe nanocrystals along with the Se loss, which is distinctly different from the phase transformations in the other TMDCs without a nonlayered stable 1:1 metal : chalcogen intermediate phase.[91] As shown in Fig. 11(m), Zhu *et al.* reported the structure and evolution of P-substituted $CoSe_2$ bifunctional electrocatalysts for HER and OER in alkaline electrolytes in real time via *in situ* liquid-phase STEM (LP-STEM). According to the *in situ* STEM and HRTEM images

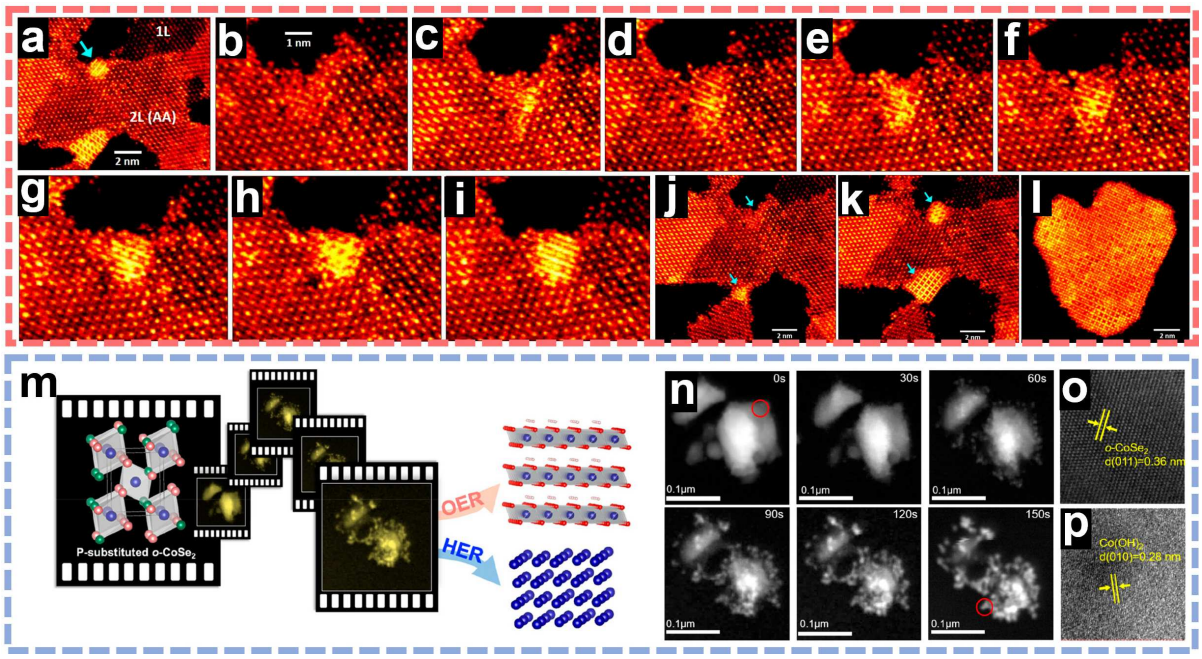


Fig. 11. Application of *in situ* STEM in TMDCs. [(a)–(l)] Phase transition from $PtSe_2$ to PtSe during *in situ* heating. (a) A starting position of the phase transition denoted by a cyan arrow pointing a PtSe nano crystal at the edge of bilayer $PtSe_2$. [(b)–(i)] Successive ADF-STEM images at the starting position with time interval of $\sim$ 30 s. [(j)–(l)] Phase transition process from the edge of the bilayer $PtSe_2$ to perfectly transformed PtSe nanoparticle after the heating. (Ref. [91] Copyright 2019, American Chemical Society). (m) Illustration of the structural evolution of P-substituted $CoSe_2$ electrocatalyst and active site identification during water electrocatalysis with LP-TEM in a KOH solution. (n) HAADF-STEM images of *in situ* reaction process. [(o) and (p)] HRTEM images of o-$CoSe_2$ and $Co(OH)_2$ for the initial and final states of the catalysts cycled in panel (n). (Ref. [92] Copyright 2019, American Chemical Society).

in Figs. 11(n)–11(p), the P-substituted $CoSe_2$ electrocatalyst in alkaline electrolyte decomposed to $Co(OH)_2$ after contact with the electrolyte. The results from *in situ* TEM revealed that P-substituted $CoSe_2$ was a "pre-catalyst" rather than a real reactive substance. The introduction of phosphorus created more vacancies and defects around Co cation in the initial $CoSe_2$ and thus greatly promoted the structural transformation to "true active substances" such as cobalt metal for HER and cobalt oxyhydroxide for OER.[92]

Hu *et al.* modeled on a series of Ni–Co bimetallic sulphides, and established an explicit and comprehensive picture of their dynamic phase evolution pathway at the precatalytic stage before OER process. At the precatalytic potential of 0.9 V, the fractional sulfur atoms on the surface of the $(NiCo)S_{1.33}$ particles were partially replaced by oxygen in the electrolyte, and the crystal structure remained unchanged, which further induced the formation of the fractional oxygen–sulfur coexistence surface $(NiCo)O_xS_{1.33-x}$. The surface of $(NiCo)O_xS_{1.33-x}$ can significantly increase the lattice oxygen oxidation mechanism ratio of the sulfide matrix and contributes to the catalytic activity, which reduces the energy barrier of surface reconstitution to NiCo-oxy/hydroxide as an active electrocatalyst and facilitates the OER process.[93] For the water electrolysis process, surface reconstruction is ubiquitous, but there is still a lack of experimental observations and mechanistic explanations. Fu *et al.* studied the surface reconstruction of Ru dopped 2D metal phosphorus trichalcogenides nanosheets in alkaline electrolysis of water for hydrogen production. *In situ* electrochemical TEM revealed that the inevitable surface reconstruction induced the *in situ* formation of $NiPS_3$ amorphous layer, which can stabilize the doped Ru single atoms and thus effectively reduce the reaction energy barrier.[94] These examples above suggest the vital potential of *in situ* electrochemical TEM for revealing the catalytic mechanisms and optimizing catalytic activities of TMDC electrocatalysts.

6. Summary and perspective

In this review, the recent progress in TMDCs for electrocatalysis is summarized in terms of controlled preparation, structure characterization, and performance modulation. Meanwhile, remarkable progresses of C_s corrected STEM with new imaging and spectroscopy techniques are summarized, and their successful applications with respect to identifying the active sites of TMDCs are discussed. In the end, we discuss the development of *in situ* electron microscopy and its application in TMDCs materials.

Although considerable progress has been achieved in TMDCs, various challenges still need to be faced for practical application. Firstly, the construction of highly active phases in nano catalysts has brought about an inevitable problem because of their metastable state, which limits their large-scale application. Secondly, sophisticated experiments and more comprehensive analyses are needed to bridge the active sites resolved by advanced TEM and STEM at atomic level with the macroscopic performances of TMDC electrocatalysts. On the other hand, as claimed by Pennycook, although atomic resolution has been achieved on the projection plane of a crystalline material, the atomic resolution on depth of the electron beam is still restricted. The resolution along the beam direction can be manipulated in STEM by convergence angle.[95] What is more, the currently fast developed artificial intelligence (AI) driven image analysis method may help automatically analyze and recognize various active sites of TMDCs, such as phases, heteroatoms, vacancies, strains, etc.[96] Meanwhile, *in situ* STEM is a spring-up field of exploring the atomic structures of materials under the operating conditions dynamically with a high temporal resolution, which can greatly expand the function of electron microscopy to a platform of linking the atomic scale characterization and the macro level of catalytic performances. In summary, TEM characterization techniques with ease of use are still challenging and need further development, but the future for advanced catalyst design and microscopy has never looked more exciting!

Acknowledgments

Project supported by the National Natural Science Foundation of China (Grant Nos. U21A20174 and 52001222), the Science and Technology Innovation Talent Team Project of Shanxi Province (Grant No. 202304051001010), the Key National Scientific and Technological Co-operation Projects of Shanxi Province (Grant No. 202104041101008), the Natural Science Foundation of Shanxi Province (Grant No. 202303021221045), the Program for the Innovative Talents of Higher Education Institutions of Shanxi (PTIT), and the Scientific and Technological Innovation Programs of Higher Education Institutions in Shanxi (STIP) (Grant No. 2022L036).

References

[1] Novoselov K S, Geim A K, Morozov S V, Jiang D, Zhang Y, Dubonos S V, Grigorieva I V and Firsov A A 2004 *Science* **306** 666
[2] Guo J, Lee J, Contescu C I, Gallego N C, Pantelides S T, Pennycook S J, Moyer B A and Chisholm M F 2014 *Nat. Commun.* **5** 5389
[3] Guo J, Morris J R, Ihm Y, Contescu C I, Gallego N C, Duscher G, Pennycook S J and Chisholm M F 2012 *Small* **8** 3283
[4] Zhang X, Guo J, Guan P, Liu C, Huang H, Xue F, Dong X, Pennycook S J and Chisholm M F 2013 *Nat. Commun.* **4** 1924
[5] Liu P, Tian H, Windl W, Gu G, Duscher G, Wu Y, Zhao M, Guo J, Xu B and Liu L 2019 *Nanoscale* **11** 20676
[6] Pei L, Yang L, Cao H, Liu P, Zhao M, Xu B and Guo J 2020 *Electrochim. Acta* **364** 137313
[7] Song Y, Sha W, Song M, Liu P, Tian J, Wei H, Hao X, Xu B, Guo J and Liang J 2021 *Ceram. Int.* **47** 19098

[8] Xiao H, Chi K, Yin H, Zhou X, Lei P, Liu P, Fang J, Li X, Yuan S, Zhang Z, Su Y, Guo J and Qian L 2024 *Energy Environ. Mater.* **7** e12495

[9] Song Y, Song M, Liu P, Liu W, Yuan L, Hao X, Pei L, Xu B, Guo J and Sun Z 2021 *J. Mater. Chem. A* **9** 14372

[10] Lu Z, Wang J, Zhang P, Guo W, Shen Y, Liu P, Ji J, Du H, Zhao M, Liang H and Guo J 2024 *Appl. Catal. B-Environ.* **353** 124073

[11] Zhang Z, Wang Z, Zhang H, Zhang Z, Zhou J, Hou Y, Liu P, Xu B, Zhang H and Guo J 2023 *J. Mater. Chem. A* **11** 4355

[12] Song Y, Xu B, Liao T, Guo J, Wu Y and Sun Z 2020 *Small* **17** 2002240

[13] Fu Q, Han J, Wang X, Xu P, Yao T, Zhong J, Zhong W, Liu S, Gao T, Zhang Z, Xu L and Song B 2020 *Adv. Mater.* **33** 1907818

[14] Zhang Z, Liu W, Zhang B, Sateesh B, Yuan L, Zhu D, Guan P, Pennycook S J and Guo J 2021 *2D Mater.* **8** 025017

[15] Mawlong L P L and Ahn J H 2021 *Small Struct.* **3** 2100149

[16] Nutting D, Prando G A, Severijnen M, Barcelos I D, Guo S, Christianen P C M, Zeitler U, Galvão Gobato Y and Withers F 2021 *Nanoscale* **13** 15853

[17] Dutta A, Breuer O, Krishnappa M, Minnes R, Zak A and Borenstein A 2023 *J. Mater. Chem. A* **11** 21806

[18] Yang L, Yang X, Yu L and Lv R 2020 *Chem Asian J.* **15** 3682

[19] Duan X, Xu J, Wei Z, Ma J, Guo S, Liu H and Dou S 2017 *Small Methods* **1** 1700156

[20] Xiu L, Pei W, Zhou S, Wang Z, Yang P, Zhao J and Qiu J 2020 *Adv. Funct. Mater.* **30** 1910028

[21] Zinatloo-Ajabshir S, Morassaei M S, Amiri O, Salavati-Niasari M and Foong L K 2020 *Ceram. Int.* **46** 17186

[22] Wang J, Guo B, Sun J, Zhou Y, Zhao C, Wei Z and Guo J 2023 *Appl. Catal. B-Environ.* **324** 122169

[23] Guo J, Mao Z, Yan X, Su R, Guan P, Xu B, Zhang X, Qin G and Pennycook S J 2016 *Nano Energy* **28** 261

[24] Tu H, Zhang H, Song Y, Liu P, Hou Y, Xu B, Liao T, Guo J and Sun Z 2023 *Adv. Sci.* **10** 2305194

[25] Tian Z, Song Y, Gan M, Shen Y, Zhang P, Liu P, Liu C, Xu B and Guo J 2024 *Appl. Surf. Sci.* **661** 160065

[26] Zhang Z, Liu P, Song Y, Hou Y, Xu B, Liao T, Zhang H, Guo J and Sun Z 2022 *Adv. Sci.* **9** 2204297

[27] Tian J, Shen Y, Liu P, Zhang H, Xu B, Song Y, Liang J and Guo J 2022 *J. Mater. Sci. Technol.* **127** 1

[28] Luo R, Gao M, Wang C, Zhu J, Guzman R and Zhou W 2023 *Adv. Funct. Mater.* **34** 2307625

[29] Wu L and Hofmann J P 2021 *ACS Energy Lett.* **6** 2619

[30] Coogan Á and Gun'ko Y K 2021 *Mater. Adv.* **2** 146

[31] Wang X, Cao X, Ding E, Yin M, Huang L and Zhang L 2024 *Carbon* **221** 118887

[32] Chen B, Hu P, Yang F, Hua X, Yang F F, Zhu F, Sun R, Hao K, Wang K and Yin Z 2023 *Small* **19** 2207177

[33] Wei Y, Liu X, Zhang Y, Yao R, Zhai T and Li H 2022 *ACS Appl. Energy Mater.* **5** 14550

[34] Zheng M, Pan Q, Gong F and Li C 2023 *Diamond Relat. Mater.* **136** 109982

[35] Huang J, Liu Y, Yan P, Gao J, Fan Y and Jiang W 2022 *J. Materiomics* **8** 790

[36] Yang H, Zhao Y, Wen Q, Mi Y, Liu Y, Li H and Zhai T 2021 *Nano Res.* **14** 4814

[37] Fu Q, Dai J Q, Huang X Y, Dai Y Y, Pan Y H, Yang L L, Sun Z Y, Miao T M, Zhou M F, Zhao L, Zhao W J, Han X, Lu J P, Gao H J, Zhou X J, Wang Y L, Ni Z H, Ji W and Huang Y 2022 *Adv. Sci.* **9** 2204247

[38] Hu B, Wu Y, Wang K, Guo H, Lei Z, Liu Z and Wang L 2023 *Small* **20** 2305344

[39] Pan X, Yan M, Sun C, Zhao K, Luo W, Hong X, Zhao Y, Xu L and Mai L 2020 *Adv. Funct. Mater.* **31** 2007840

[40] Kang B H, Shin S, Nam K, Bae J, Oh J M, Koo S M, Sohn H, Park S H and Shin W H 2023 *J. Mater. Chem. A* **11** 19083

[41] Wang S, Huang J K, Li M, Azam A, Zu X, Qiao L, Yang J and Li S 2021 *ACS Appl. Mater. Interfaces* **13** 47962

[42] Chen M, Zhang A, Liu Y, Cui D, Li Z, Chung Y H, Mutyala S P, Mecklenburg M, Nie X, Xu C, Wu F, Liu Q and Zhou C 2020 *Nano Res.* **13** 2625

[43] Ma H, Qian Q, Qin B, Wan Z, Wu R, Zhao B, Zhang H, Zhang Z, Li J, Zhang Z, Li B, Wang L and Duan X 2021 *Adv. Sci.* **9** 2103507

[44] Zhou J, Lin J, Huang X, Zhou Y, Chen Y, Xia J, Wang H, Xie Y, Yu H, Lei J, Wu D, Liu F, Fu Q, Zeng Q, Hsu C H, Yang C, Lu L, Yu T, Shen Z, Lin H, Yakobson B I, Liu Q, Suenaga K, Liu G and Liu Z 2018 *Nature* **556** 355

[45] Zhang J, Li Y, Liang X, Liu Q, Chen Q and Chen M 2021 *Small* **18** 2106074

[46] Zhang Y, Yang T, Li J, Zhang Q, Li B and Gao M 2022 *Adv. Funct. Mater.* **33** 2210939

[47] Wang G, Zhang G, Ke X, Chen X, Chen X, Wang Y, Huang G, Dong J, Chu S and Sui M 2022 *Small* **18** 2107238

[48] Nellist P D and Pennycook S J 1999 *Ultramicroscopy* **78** 111

[49] Liu P Z, Hao B, Zhang H X, Xu B S and Guo J J 2021 *New Carbon Materials* **36** 497

[50] Pennycook S J and Boatner L A 1988 *Nature* **336** 565

[51] Pennycook S J and Jesson D E 1990 *Phys. Rev. Lett.* **64** 938

[52] Browning N D, Chisholm M F and Pennycook S J 1994 *Adv. Mater.* **6** 328

[53] Nellist P D, Chisholm M F, Dellby N, Krivanek O L and Pennycook S J 2004 *Science* **305** 1741

[54] Batson, P. E, Dellby, N., Krivanek, O. and L. 2002 *Nature* **418** 617

[55] Krivanek O L, Chisholm M F, Nicolosi V, Pennycook T J, Corbin G J, Dellby N, Murfitt M F, Own C S, Szilagyi Z S and Oxley M P 2010 *Nature* **464** 571

[56] Suenaga K and Koshino M 2010 *Nature* **468** 1088

[57] Erni R, Rossell M D, Kisielowski C and Dahmen U 2009 *Phys. Rev. Lett.* **102** 096101

[58] Ge J, Chen Y, Zhao Y, Wang Y, Zhang F and Lei X 2022 *ACS Appl. Mater. Interfaces* **14** 26846

[59] Shao G, Xu J, Gao S, Zhang Z, Liu S, Zhang X and Zhou Z 2023 *Carbon Energy* **6** e417

[60] Ji X, Ding D, Guan X, Wu C, Qian H, Cao J, Li J and Jin C 2021 *ACS Nano* **15** 15039

[61] Zhang C, Chuu C P, Ren X, Li M Y, Li L J, Jin C, Chou M Y and Shih C K 2017 *Sci. Adv.* **3** e1601459

[62] Zhu H, Gao G, Du M, Zhou J, Wang K, Wu W, Chen X, Li Y, Ma P, Dong W, Duan F, Chen M, Wu G, Wu J, Yang H and Guo S 2018 *Adv. Mater.* **30** 201707301

[63] Gong X, Jiang Z, Zeng W, Hu C, Luo X, Lei W and Yuan C 2022 *Nano Lett.* **22** 9411

[64] Qin J, Xi C, Zhang R, Liu T, Zou P, Wu D, Guo Q, Mao J, Xin H and Yang J 2021 *ACS Catal.* **11** 4486

[65] Sun K, Liu Y, Pan Y, Zhu H, Zhao J, Zeng L, Liu Z and Liu C 2018 *Nano Res.* **11** 4368

[66] Pam M E, Hu J, Ang Y S, Huang S, Kong D, Shi Y, Zhao X, Geng D, Pennycook S J, Ang L K and Yang H Y 2019 *ACS Appl. Mater. Interfaces* **11** 34862

[67] Shi J, Huan Y, Hong M, Xu R, Yang P, Zhang Z, Zou X and Zhang Y 2019 *ACS Nano* **13** 8442

[68] Vikraman D, Hussain S, Karuppasamy K, Feroze A, Kathalingam A, Sanmugam A, Chun S H, Jung J and Kim H S 2020 *Appl. Catal. B-Environ.* **264** 118531

[69] Xu H M, Gu C, Zhang X L, Shi L, Gao Q, Hu S, Han S K, Zheng X, Gao M R and Yu S H 2021 *CCS Chem.* **3** 58

[70] Sun Y, Li X, Zhang T, Xu K, Yang Y, Chen G, Li C and Xie Y 2021 *Angew. Chem., Int. Ed.* **60** 21575

[71] Ping X, Liang D, Wu Y, Yan X, Zhou S, Hu D, Pan X, Lu P and Jiao L 2021 *Nano Lett.* **21** 3857

[72] Zhang J, Li J, Huang H, Chen W, Cui Y, Li Y, Mao W, Zhu X and Li X A 2022 *Small* **18** 2204557

[73] Medda A, Biswas R, Dastider S G, Ghosh S, Mondal K, Haldar K K and Patra A 2023 *ACS Appl. Energy Mater.* **6** 11745

[74] Yun S, Gao Z, Yang T, Sun M, Yang G, Wang K, Wang Z, Yuan S and Zhang M 2023 *Adv. Funct. Mater.* **34** 2314226

[75] Peng Y, Zhu L, Li C, Hu J, Lu Y, Fu J, Cui F, Wang X, Cao A, Ji Q, Huan Y and Zhang Y 2023 *Adv. Energy Mater.* **14** 2302510

[76] Xia L, Pan K, Wu H, Wang F, Liu Y, Xu Y, Dong Z, Wei B and Wei S 2022 *ACS Appl. Mater. Interfaces* **14** 22030

[77] Wu T, Song E, Zhang S, Luo M, Zhao C, Zhao W, Liu J and Huang F 2022 *Adv. Mater.* **34** 2108505

[78] Chang Y, Zhai P, Hou J, Zhao J and Gao J 2021 *Adv. Energy Mater.* **12** 2102359

[79] Zheng H, Wang S, Liu S, Wu J, Guan J, Li Q, Wang Y, Tao Y, Hu S, Bai Y, Wang J, Xiong X, Xiong Y and Lei Y 2023 *Adv. Funct. Mater.* **33** 2300815

[80] Meng H, Liu X, Chen X, Han Y, Zhou C, Jiang Q, Tan T and Zhang R 2022 *J. Energy Chem.* **71** 528
[81] Liu Z, Li N, Su C, Zhao H, Xu L, Yin Z, Li J and Du Y 2018 *Nano Energy* **50** 176
[82] Han A, Zhou X, Wang X, Liu S, Xiong Q, Zhang Q, Gu L, Zhuang Z, Zhang W, Li F, Wang D, Li L J and Li Y 2021 *Nat. Commun.* **12** 709
[83] Zheng Z, Yu L, Gao M, Chen X, Zhou W, Ma C, Wu L, Zhu J, Meng X, Hu J, Tu Y, Wu S, Mao J, Tian Z and Deng D 2020 *Nat. Commun.* **11** 3315
[84] Zhang J, Xu X, Yang L, Cheng D and Cao D 2019 *Small Methods* **3** 1900653
[85] Yang J, Wang Y, Lagos M J, Manichev V, Fullon R, Song X, Voiry D, Chakraborty S, Zhang W, Batson P E, Feldman L, Gustafsson T and Chhowalla M 2019 *ACS Nano* **13** 9958
[86] Zhou Y, Song E, Zhou J, Lin J, Ma R, Wang Y, Qiu W, Shen R, Suenaga K, Liu Q, Wang J, Liu Z and Liu J 2018 *ACS Nano* **12** 4486
[87] Wu Q, Luo Y, Xie R, Nong H, Cai Z, Tang L, Tan J, Feng S, Zhao S, Yu Q, Lin J, Chai G and Liu B 2022 *Small* **18** 2201051
[88] Gao B, Du X, Zhao Y, Seok Cheon W, Ding S, Xiao C, Song Z and Won Jang H 2022 *Chem. Eng. J.* **433** 133768
[89] Liu X, Xiao J, Peng H, Hong X, Chan K and Nørskov J K 2017 *Nat. Commun.* **8** 15438
[90] Lin J, Cretu O, Zhou W, Suenaga K, Prasai D, Bolotin K I, Cuong N T, Otani M, Okada S, Lupini A R, Idrobo J C, Caudel D, Burger A, Ghimire N J, Yan J, Mandrus D G, Pennycook S J and Pantelides S T 2014 *Nat. Nanotechnol.* **9** 436
[91] Ryu G H, Chen J, Wen Y and Warner J H 2019 *Chem. Mater.* **31** 9895
[92] Zhu Y, Chen H C, Hsu C S, Lin T S, Chang C J, Chang S C, Tsai L D and Chen H M 2019 *ACS Energy Lett.* **4** 987
[93] Hu Y, Zheng Y, Jin J, Wang Y, Peng Y, Yin J, Shen W, Hou Y, Zhu L, An L, Lu M, Xi P and Yan C 2023 *Nat. Commun.* **14** 1949
[94] Fu Q, Wong L W, Zheng F, Zheng X, Tsang C S, Lai K H, Shen W, Ly T H, Deng Q and Zhao J 2023 *Nat. Commun.* **14** 6462
[95] Liu P, Xu B and Guo J 2015 *J. Chin. Electr. Microsc. Soc.* **34** 371
[96] Dan J, Zhao X, Ning S, Lu J, Loh K P, He Q, Loh N D and Pennycook S J 2022 *Sci. Adv.* **8** eabk1005